

Review

# A Review of Three-Dimensional Scanning Near-Field Optical Microscopy (3D-SNOM) and Its Applications in Nanoscale Light Management

Paul Bazylewski, Sabastine Ezugwu  and Giovanni Fanchini \* 

Department of Physics and Astronomy, University of Western Ontario, London, ON N6A3K7, Canada; pbazylew@uwo.ca (P.B.); sezugwu@uwo.ca (S.E.)

\* Correspondence: gfanchin@uwo.ca; Tel.: +1-519-661-2111

Received: 21 June 2017; Accepted: 14 July 2017; Published: 22 September 2017

**Abstract:** In this article, we present an overview of aperture and apertureless type scanning near-field optical microscopy (SNOM) techniques that have been developed, with a focus on three-dimensional (3D) SNOM methods. 3D SNOM has been undertaken to image the local distribution (within ~100 nm of the surface) of the electromagnetic radiation scattered by random and deterministic arrays of metal nanostructures or photonic crystal waveguides. Individual metal nanoparticles and metal nanoparticle arrays exhibit unique effects under light illumination, including plasmon resonance and waveguiding properties, which can be directly investigated using 3D-SNOM. In the second part of this article, we will review a few applications in which 3D-SNOM has proven to be useful for designing and understanding specific nano-optoelectronic structures. Examples include the analysis of the nano-optical response phonetic crystal waveguides, aperture antennae and metal nanoparticle arrays, as well as the design of plasmonic solar cells incorporating random arrays of copper nanoparticles as an optical absorption enhancement layer, and the use of 3D-SNOM to probe multiple components of the electric and magnetic near-fields without requiring specially designed probe tips. A common denominator of these examples is the added value provided by 3D-SNOM in predicting the properties-performance relationship of nanostructured systems.

**Keywords:** scanning near-field optical microscopy; c-SNOM; s-SNOM; nanoscale imaging; nanoparticles; 3D SNOM

---

## 1. Introduction

Imaging of nanoscale features has been a long standing challenge in optical microscopy. In the late 19th century an apparent fundamental limit on the maximum resolution of an optical image was formulated based on the diffraction theory of light [1]. Although this formulation suggested that optical microscopy was limited to micron-scale objects, the diffraction limit has since been overcome through the development of super resolution techniques operating in the far-field [1–7]. Far-field super resolution strategies make use of enhanced contrast using a secondary process such as fluorescence or scattering to image subwavelength nanostructures. Fluorescence imaging was one of the first super resolution techniques to be developed. It utilizes fluorescence emitted from a fluorophore used to mark a sample rather than diffracted light, allowing for nanoscale images to be produced down to single-molecule resolution [2]. Fluorescence imaging forms the backbone of super resolution techniques capable of nanoscale imaging, that includes stimulated emission depletion (STED) microscopy, photo-activated localization microscopy, structured illumination spectroscopy, and stochastic optical reconstruction microscopy (STORM) [2,6,7]. STED is a variation of fluorescence imaging that achieves higher resolution by selectively quenching fluorophores used for labeling. Through judicious choice of fluorophore and excitation laser, resolution in the tens of nanometers

can be achieved [2]. STORM employs a variation of STED utilizing time-resolved selective switching of fluorophores. Selective switching in this manner is used to collect a series of images that can be combined to produce images with nanometer resolution. Through careful choice of measurement optics, STORM can also be used to detect fluorescence from below a sample surface to construct 3D images [7]. The major drawback to any fluorescence based technique is the potential for photo bleaching and sample damage brought on by the requirement for highly focused light sources.

Diffraction limited resolution can be avoided without the need for sample labeling, and the dangers of photo bleaching though the use of scattering techniques such as optical coherence tomography (OCT) which can achieve sub-micron resolution [3–5]. Researchers realized that OCT could be enhanced with interferometry, which combines a series of images to produce an interference pattern containing information about sub-wavelength surface features. OCT typically employs longer wavelength light which has the added benefit of penetrating deeply into biological tissue. This gives OCT the ability to collect 3D images at depths of hundreds of microns beneath a sample's surface [4]. Light scattering techniques of this type are advantageous over fluorescence in that no labeling of the samples are necessary, but at the cost of lower resolving power. Scanning near-field microscopy (SNOM or NSOM) is the most recently developed super resolution technique based on light scattering that is also capable of obtaining nanoscale images.

SNOM is a photon-in photon-out nano-optical imaging technique that uses near-field light to construct nanoscale images. To make use of the near-field, a nanoscale probe is brought into the near-field of a surface or object to be investigated, causing near-field evanescent waves to be scattered into the far-field to be detected. Evanescent light experiences an exponential decay in the propagation direction away from the originating surface that has the consequence of localizing the near-field to a volume within  $\sim 100$  nm nanometers of the originating emitter. This localization produces a high intensity near-field very near the surface, which contains information about the surface properties beyond the diffraction-limited maximum resolution of the far-field. In this way, SNOM can be used to acquire super resolution optical images by scanning a probe tip over a surface in two dimensions, or mapping the entire near-field of a surface by scanning in three dimensions.

Although SNOM is a nanoscale and contactless technique that does not require any fluorophore labeling and is not subject to the issue of photo bleaching, it possesses other considerable challenges. Probing the near-field of a surface makes it necessary to bring a nanoscale object within the near-field of the surface. This requires finely machined tips that are most often coupled to an atomic force microscope (AFM) system that allows three dimensional movement of the tip with nanometer resolution. This requirement also makes SNOM primarily a surface technique compared to the depth profiling possible with fluorescence labeling. The near-field light emitted from a sample is only capable of propagating a short distance away from the emitting source, which minimizes the depth profiling ability of SNOM.

This review article provides an overview of recent studies using the two different modes of SNOM, aperture and apertureless, that have been applied for the characterization of thin films, nano particles, and devices. The basic theory of SNOM, as well as the differences between the two basic SNOM modes, apertureless and aperture-type, are presented in Section 2. Advances in aperture-type SNOM, defined as mapping of electric and magnetic fields associated to scattering of electromagnetic radiation in the near-field by a particle in the proximity of a nano-aperture are reviewed in Section 3. Imaging using apertureless SNOM, defined as detection of electromagnetic radiation scattered by a particle by using another particle (typically: a scanning probe tip) is presented in Section 4, along with how SNOM has enabled mapping of otherwise inaccessible electromagnetic near-field properties. The final part of this article, Section 5, reviews the use of SNOM in a three-dimensional scanning arrangement. Typically, SNOM measurements are performed by raster scanning the SNOM tip in a two dimensional ( $x, y$ ) scan while carefully controlling the height of the tip above the surface. As an extension of this type of scanning, 3D SNOM includes additional ( $x, y$ ) scans moving the probe away from the surface in the

z-direction, and has been used to study light scattering near surfaces that is otherwise inaccessible by other techniques.

## 2. Types of SNOM Methods

Any monochromatic light field can be represented by a vector field  $E(r)$  (similarly for the magnetic component,  $H(r)$ ) containing components  $A_m(r)$  and  $\varphi_m(r)$  that represent the spatially dependent amplitude and phase of the vector components of the field ( $m = x, y, z$  in Cartesian coordinates). The field can be represented by a set of waves of the form shown below.

$$E(r) = \int_{-\infty}^{+\infty} E_k e^{ik \cdot r} dk \quad (1)$$

where  $r$  represents spatial position, and each wave in the set is defined by its wavevector  $k$  and complex amplitude  $E_k$ . For a given far-field distribution in a non-absorbing medium with real index of refraction  $n$ , wavevector  $k$  is real with an amplitude defined by  $k_o = \sqrt{k_x^2 + k_y^2 + k_z^2} = 2\pi n / \lambda$ , and wavelength in vacuum,  $\lambda$ . However, if  $k_x^2 + k_y^2 > k_o^2 = \omega^2 / c^2$ , then  $k_z$  must have a non-zero imaginary component. From Equation (1), any imaginary components within the far-field wavevector  $k$  will result in an exponentially decaying amplitude. A light wave defined by such exponential decay is termed an evanescent wave, and it experiences an exponential decay in amplitude moving away from its originating location. The exponential decay in the propagation direction away from the originating surface has the consequence of localizing the near-field to the originating emitter structure or interface (within a distance less than 100 nm from the surface), which also results in the light field near a surface being dominated by evanescent light [8]. A consequence of this is the real part of the wavevectors  $k_n$  is larger than  $k_o$ , resulting in a near-field structure that contains information about the surface beyond the diffraction-limited maximum resolution of the far-field.

Figure 1a illustrates the contrast between imaging in the far and near-fields; to make use of near-field light the SNOM probe must be positioned within the near-field, close to the sample surface at a distance  $r$  much less than the wavelength,  $\lambda$ , of the incident light. For this reason, SNOM is typically demonstrated in practice coupled to a scanning microscopy system such as AFM. The cantilever system of an AFM allows the SNOM tip to be positioned very close to the surface at a distance of tens of nm ( $r \ll \lambda$ ), to be within the near-field as shown in Figure 1a,b. The sample is then scanned in a raster pattern to map the near-field distribution while maintaining a tip position very close to the surface. Coupling to an AFM system also allows for simultaneous collection of a topography image and a SNOM image, providing a method to map the surface nanoscale morphology directly to the optical and chemical properties observed in the SNOM image.

Two distinct modes of SNOM imaging have been employed, and are classified by the type of tip that is used. Aperture SNOM, also called collection SNOM (c-SNOM), uses hollowed out tips that allow light to shine from the back out of, or up into, the tip as shown in Figure 1b. Aperture tips function by generating near-field light by scattering of far-field light from the nanoscale aperture at the end of the tip. The generated tip near-field is subsequently scattered off the sample surface, into the far-field to be detected. Early versions of the SNOM technique employed a tapered optical fiber with a metallic tip and a subwavelength opening for this purpose [1,8]. The standard aperture tip possesses a circular opening with a typical diameter ranging from 80 to 250 nm, but can be as small as 10–20 nm using advanced nanofabrication procedures. The particular size and shape of the tip and aperture, as well as the tip composition dictate the range of frequencies that can be coupled to or scattered by the sample. In this fashion designer tips have been fabricated with a desired aperture size and shape to improve SNOM performance by increasing resolution, maximizing transmission [9,10], or providing access to more exotic features such as magnetic near-fields using a bowtie, split ring, or pyramidal (campanile) shape [10,11].

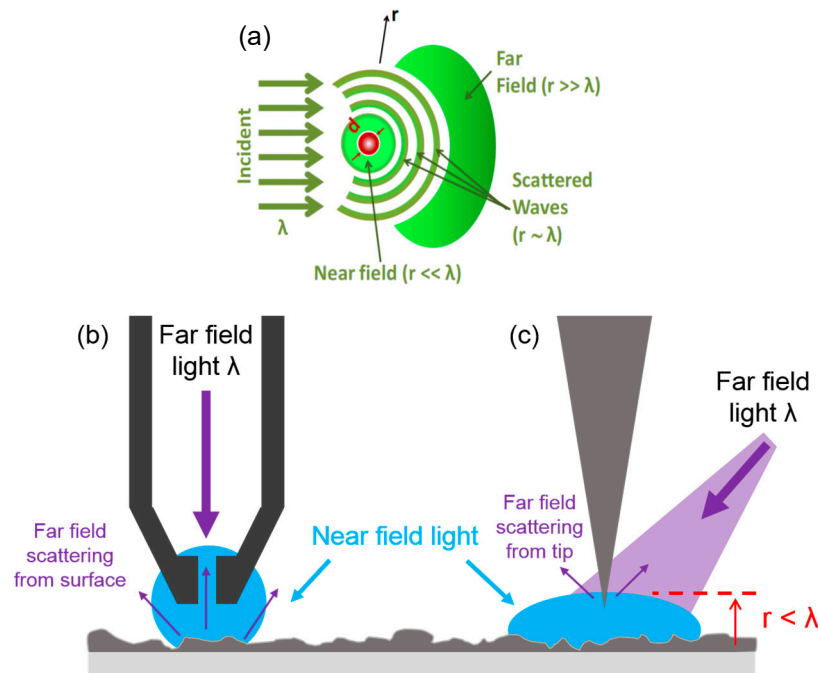


**Figure 1.** The near-field and types of SNOM tips. (a) The far and near-field microscopy arrangements are defined by the proximity of the probe to the nano object being probed. When at a distance ( $r$ ) from the emitting object that is much less than the wavelength of light used, evanescent light dominates the light field; (b) Aperture SNOM where an evanescent light field created by a nanoscale opening at the end of a tip is scattered off of the surface. Light scattered from the surface is detected in the far-field; (c) Apertureless SNOM utilizes near-field light emitted from the surface due to external illumination that is scattered off of a sharp tip into the far-field to be detected.

Although there are a large number of applications that utilize c-SNOM, some significant limitations of this technique remain; (1) low light transmission through the aperture, and (2) a fundamental lower limit of aperture size of approximately 10 nm due to the skin depth of metals [12]. Poor light transmission through the tip aperture can be overcome through the use of high brightness light sources such as lasers, while the lower limit on aperture size can be circumvented through the use of apertureless tips. Apertureless-type SNOM systems, or scattering SNOM (s-SNOM), utilize light from an external source scattered from an apertureless tip which acts as an antenna to produce a source of evanescent light near the nanostructured sample surface as shown in Figure 1c. Apertureless-type operation is advantageous in that it does not suffer from the fundamental size limitations of c-SNOM, and can achieve resolution below 10 nm [1,8,13]. However, apertureless-type SNOM systems are more challenging to implement than their aperture-type counterparts. This is due to a relatively intense far-field background composed of light reflected or scattered directly from the sample surface. This unavoidably creates a large background signal over a spatial area much larger than the near-field domain of the tip [14]. The background signal is additionally subject to artifacts if the tip-sample distance is not very carefully controlled, making correct interpretation of apertureless SNOM images more difficult [15].

### 3. Aperture-Type SNOM

#### 3.1. c-SNOM Spectroscopy

In aperture-type near-field microscopy, near-field radiation can be collected through the probe tip where the size and shape of the aperture, as well as the composition of the tip can be tailored towards the specific application over a wide range of wavelengths (200–1700 nm). This allows a host of

different spectroscopy techniques to be implemented alongside SNOM systems to allow spectroscopy and imaging at sub-wavelength resolution. Techniques with which aperture-type SNOM has been coupled include Fourier-transform infrared spectroscopy (FTIR) [8], fluorescence [16], and Raman spectroscopy [17,18].

The lateral resolution of fluorescence from single molecules can be enhanced through near-field imaging of strong fluorescent emitters. Fluorescence SNOM microscopy has been very successful as a contrast method to enhance resolution using transmission, reflection, or phase contrast modes [19,20]. In Fluorescence microscopy, fluorophores such as engineered organic fluorescent molecules [21] or fluorescent proteins [22] possessing different characteristic absorption and emission wavelengths are used to label different parts of a sample. The ability to distinguish the contrast between fluorescent signals in a given sample then depends on the type of optics and detector used to collect the image. SNOM techniques have been employed as a natural extension of far-field microscopy to increase the resolution, and c-SNOM has been employed in biological, thin film, and device imaging [23,24].

Aperture-type SNOM has also been applied with great success in Raman spectroscopy. Although a review on SNOM Raman is beyond the scopes of this article, we cannot omit to report that much research has been focused on increasing the Raman cross-section to the single molecule detection limit. The sensitivity can be improved greatly by combining SNOM with other techniques such as coherent anti-Stokes Raman scattering (CARS), stimulated Raman scattering [25], or tip enhanced Raman scattering (TERS) [26]. More recently surface enhanced Raman scattering (SERS) has demonstrated label-free single molecule resolution [18,27]. Coupling Raman spectroscopy with c-SNOM systems overcomes the limitations of the other sensitivity enhancing techniques and can achieve nanoscale-SNOM enhanced Raman spectroscopy [17]. Nano Raman is a c-SNOM technique making use of aperture type tips placed within the near-field of a sample to be imaged. This technique has been used to study inorganic crystals, polymer thin films, liquid-liquid interfaces at the nanoscale, as well as mapping of single molecules on surfaces [17] an investigation that is not possible with conventional far-field Raman.

### 3.2. Imaging Electrical and Magnetic Near-Fields

In addition to probing chemical and morphological properties, SNOM has shown the capability to map electromagnetic near-fields in both c-SNOM and s-SNOM modes using careful tip design. Both the amplitude and phase of the near-field can be mapped, with phase-sensitive c-SNOM measurements allowing detection of the mode properties of light as it propagates through nanoscale waveguides composed of nanoparticles or nanowires [28,29]. With these capabilities, construction of electric and magnetic vector field maps in the near-field of exotic nanostructures, nanoparticles and nano-antennas has been accomplished [8,30,31].

Several variations of electric and magnetic field mapping are available in the literature using c-SNOM, including the ability to examine either the electric or magnetic near-field components individually, or together to form the complete electromagnetic spectrum [29]. Direct mapping of electric fields near sub wavelength holes acting as nanoantennas has been demonstrated using tips with 30 nm circular apertures [30,31]. Optical mapping of magnetic fields is more challenging, and was first demonstrated using c-SNOM with a slit etched into the tip of an aperture probe [32]. Etching a slit in the side of the probe in this way converts the aperture probe into split-ring resonator. This architecture effectively converts the normally inaccessible out-of-plane component of the magnetic field ( $H_z$ ) into detectable in-plane far-field radiation ( $E_x$  or  $E_y$ ). Careful probe design has also provided access to the in-plane magnetic fields ( $H_x$  or  $H_y$ ), such as a pyramidal shaped probe that has been used to map the magnetic response of plasmonic nanoantennas shown in Figure 2a [11,33]. Scanning electron microscope (SEM) images of these plasmonic disk (320 nm) and ring (470 nm outer diameter, 300 nm inner diameter) antennas are shown in the top row of Figure 2a. The antennas were excited by an  $H_y$  magnetic dipole source, positioned 75 nm below the antennas, and SNOM imaging was used to reveal the  $|H_y|^2$  near-field distribution near the antennas. The bottom row of Figure 2a shows experimental

SNOM images for the disk and ring architectures. The disk displays a dipole mode which produces a strong plasmon excitation due to the proximity of the probe, represented by a darkened elliptical spot. For the ring, two separated dark lobes are observed on opposite edges of the ring. Both cases correspond well to the simulated field, enabling directed design of nanoantennas [33].

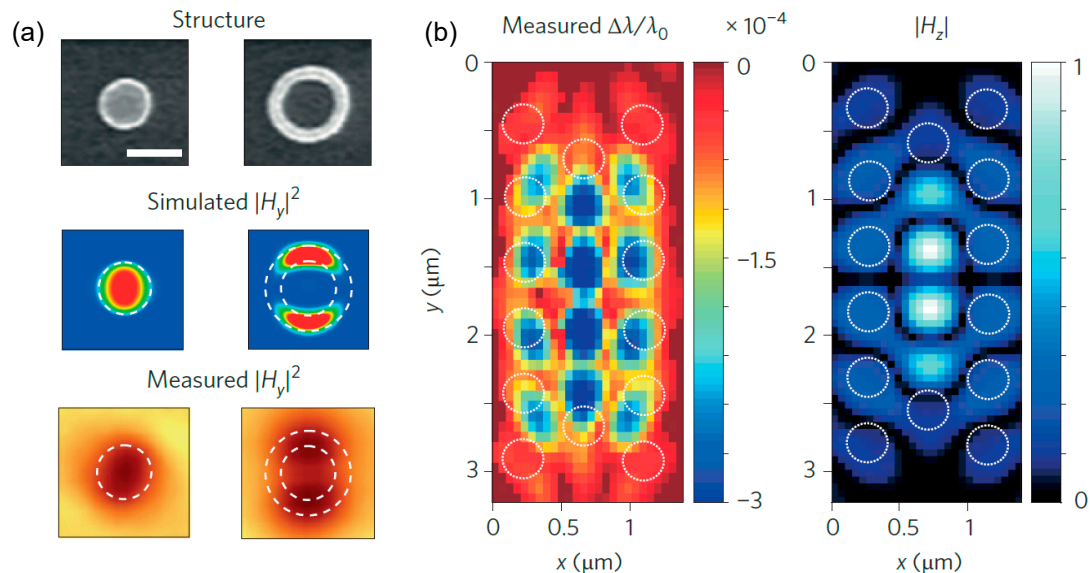


**Figure 2.** Electromagnetic near-fields probed with c-SNOM. (a) An example of magnetic near-field maps ( $H_y$ ) of single nanostructures taken with a pyramid-probe c-SNOM, scale bar is 300 nm [28]. (b) Measurements of the resonance shift of a photonic crystal nanocavity collected with a circular aperture c-SNOM probe (left). The distribution of the out-of-plane component  $H_z$  of the unperturbed cavity can be calculated from the resonance shift map (right). Reproduced with permission from [8], Copyright Nature Photonics, 2014.

The realization that an unspecialized aperture probe could be sensitive to in-plane magnetic fields indicated that the magnetic near-field could be studied in greater detail. It has been since shown that normal circular aperture c-SNOM probes can in fact be sensitive to magnetic near-fields [29,34]. Through judicious choice of aperture size and metal coating thickness, SNOM mapping of  $H_x$ ,  $H_y$  and  $E_z$  of a plane wave has been through the mapping of standing wave patterns on gold films [29]. Using photonic crystal waveguides as a test environment, c-SNOM images have shown that typical circular aperture probes are roughly equally sensitive to electric and magnetic fields, not just to the electric component [34]. The left of Figure 2b shows the use of this technique to map the in-plane map of the resonance shift in a photonic crystal nanocavity, which is made possible by the shift of the nanocavity resonance when the apex a normal circular aperture, metal coated c-SNOM probe is above an antinode of the magnetic field of the cavity [29]. The right part of Figure 2b shows the associated out-of-plane magnetic component of the light field ( $H_z$ ) that can be calculated for the unperturbed cavity [29]. These types of electromagnetic field maps are crucially important in the design and characterization of nano scale optoelectronic devices. A natural extension on the capabilities so far demonstrated for c-SNOM is to map near-fields in three dimensions, which is discussed further in Section 5 where it is used to examine the three dimensional light field of photonic crystal waveguides.

#### 4. Apertureless-Type SNOM

Imaging of electromagnetic near-fields has also been widely accomplished using non-aperture SNOM tips (Figure 1c) which can obtain higher resolution images compared to c-SNOM. The requirement for a precisely machined nano aperture is waived, but is replaced with other challenges in terms of signal detection due to a large far-field background signal from an external light source.

Photonic crystal nanocavities are a suitable test environment with well-defined nanostructures that are ideal to make use of the high resolution capabilities of s-SNOM probes [13,35–37]. Experiments examining a mid-infrared inverse bowtie antenna using s-SNOM in a polarization-resolved interferometric configuration have been used to reconstruct the near-field vector from the amplitude and phase of the electric field components ( $E_{x,y,z}$ ) [36]. Tuning of high quality factor photonic microcavities over a wide range of frequencies has been accomplished by introducing a subwavelength dielectric tip [36,37]. These cavities enable the study of tip-sample interaction to advantageously control their properties. This is made possible by varying the lateral and vertical position of the tip near the cavity, which can be used to tune the resonator frequency while maintaining the cavity quality factor [36].

The high resolution of s-SNOM that enables the study of microcavity resonators are also ideal to examine near-field effects such as surface plasmons [38–41] in graphene and metal nanostructures. Making use of IR light as the illumination source allows for collection of IR-SNOM images [42,43], and may also be coupled to FTIR spectrometer to collect high resolution spectroscopy measurements [38,44]. Imaging of plasmon effects and IR-coupled systems are discussed in the next sections.

#### 4.1. Surface Plasmon Imaging

Surface plasmon resonance is a phenomenon arising from the oscillation of free electrons near a material surface under illumination by a light source. Surface plasmons may be localized (within 10's of nanometers) on a surface due to nanostructures, or may propagate over larger areas depending on the material properties. Using a suitable excitation source, imaging of a surface using s-SNOM can reveal details about the surface plasmon distribution, as shown in Figure 3a for a wide piece graphene ribbon on an SiC substrate, and Figure 3b for a graphene ribbon tapering to a point [33]. AFM images of the same flake before and after are shown on the leftmost and rightmost edges, and the colored images show SNOM images taken with 9200 nm (left), 9681 nm (middle) and 10,152 nm (right) light wavelengths. The plasmon resonance wavelength may be tuned over a wide spectral range by adjusting the excitation wavelength used for s-SNOM in the IR spectrum. This is made possible by the dependence of the dielectric constant of the SiC substrate on the excitation wavelength. In this way, the propagation of plasmon waves over the graphene surface may be studied. In Figure 3a, fringes in the wider part of the ribbon are due to plasmon interference caused by plasmon reflections at the graphene edges. Examining the tapered ribbons shows interference fringes with a spacing that decreases with increasing SiC dielectric constant. This is due to a larger substrate permittivity yielding a smaller graphene plasmon wavelength [38]. This type of plasmon imaging can lead to improved s-SNOM performance through the design of enhanced tips. A novel application that has been proposed using graphene plasmonics is the fabrication of graphene-plasmon enhanced s-SNOM tips [39]. In this unusual approach, localized plasmons on graphene are mingled with surface plasmon polaritons to confine plasmon waves into the apex of a nearfield scanning optical microscopy tip. The tip is fabricated as a traditional metallic s-SNOM tip coated with a layer of graphene, resulting in very low loss, high resolution tips [39].

In addition to graphene, metal nanostructures have been investigated to study surface plasmon polaritons (SPP). SPPs are a type of surface wave that can be guided along a surface with applications in light generation or photonic data storage. This type of surface effect can be induced through the introduction of cross grooves fabricated in an Au thin film [40]. SPP excitation in this case was found to depend on the direction of the electric field of the incident light relative to the cross-sections of the grooves [41]. s-SNOM is uniquely suited to study plasmon activity in nano structures such as graphene because of the extremely high resolution and the requirement that the sample be illuminated by a light field to produce plasmons.

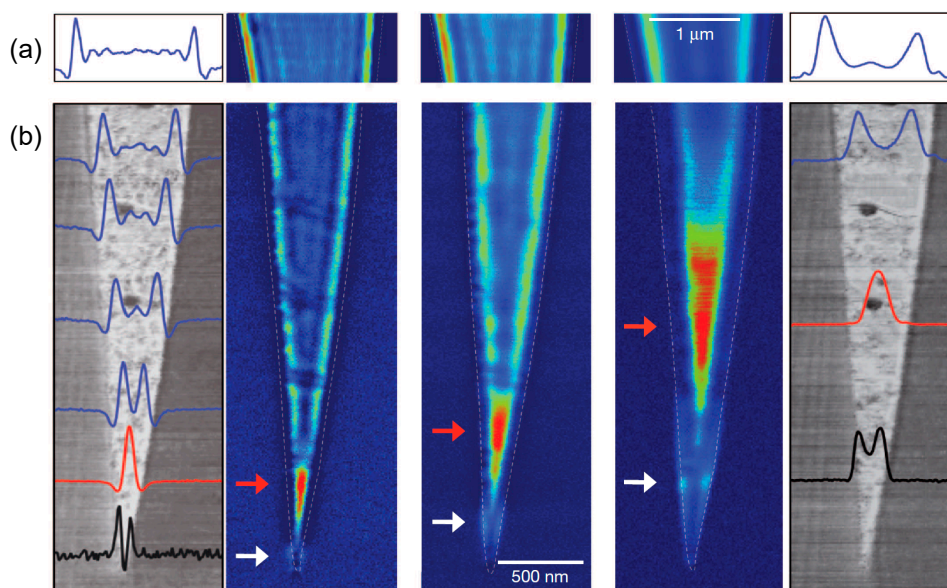


**Figure 3.** S-SNOM images of graphene plasmons. (a) 1 mm wide graphene nano ribbons on an SiC substrate. The black and white images show AFM morphology, while the colored images were taken with 9200 nm (left), 9681 nm (middle) and 10,152 nm (right) light wavelengths. The line plots on the panels at the far left and right edges represent the near-field images for  $\lambda_0 = 9200$  nm and  $\lambda_0 = 10,152$  nm; (b) Tapered graphene ribbons on the same SiC substrate imaged with SNOM, where the arrows indicate localized resonant modes. Reproduced with permission from [38], Copyright Nature, 2012.

#### 4.2. Infrared Nano-Imaging

Both infrared imaging and FTIR have been coupled to a SNOM system, and have been used successfully using s-SNOM [42–45]. In this arrangement, the sample is illuminated with far-field IR light with the resulting near-field scattered from an s-SNOM tip. In order to collect FTIR spectra, the AFM-SNOM tip arrangement need not be modified; only additional detectors and optics are required. FTIR SNOM mapping has been used to great effect on other systems including biological systems, semiconductor devices or thin film stacks may be investigated with nano-FTIR systems [38,42–44]. The high resolution of SNOM allows the structure of single proteins to be imaged [43], along with collection of a nano-FTIR of neighboring proteins.

Access to sub-wavelength features of thin films can provide otherwise inaccessible information including polymorphism or phase coexistence in organic films. Figure 4a,b depict AFM and IR s-SNOM image of a pentacene thin film recorded using mid-infrared illumination, respectively [45]. The topography image alone is not sufficient to identify two different phases of pentacene, thin film or bulk phase, where the bulk phase is associated with larger grains and poor charge carrier mobility [45]. The corresponding IR s-SNOM image however, clearly identifies a mixed phase with larger ellipsoidal grains throughout the films. This is confirmed using nano-FTIR (Figure 4c) with peak fitting which clearly identifies a shift in the resonance frequency of the bulk phase (green line, yellow ellipsoids in the image) compared to the surrounding thin film phase (blue line, red areas in the images).

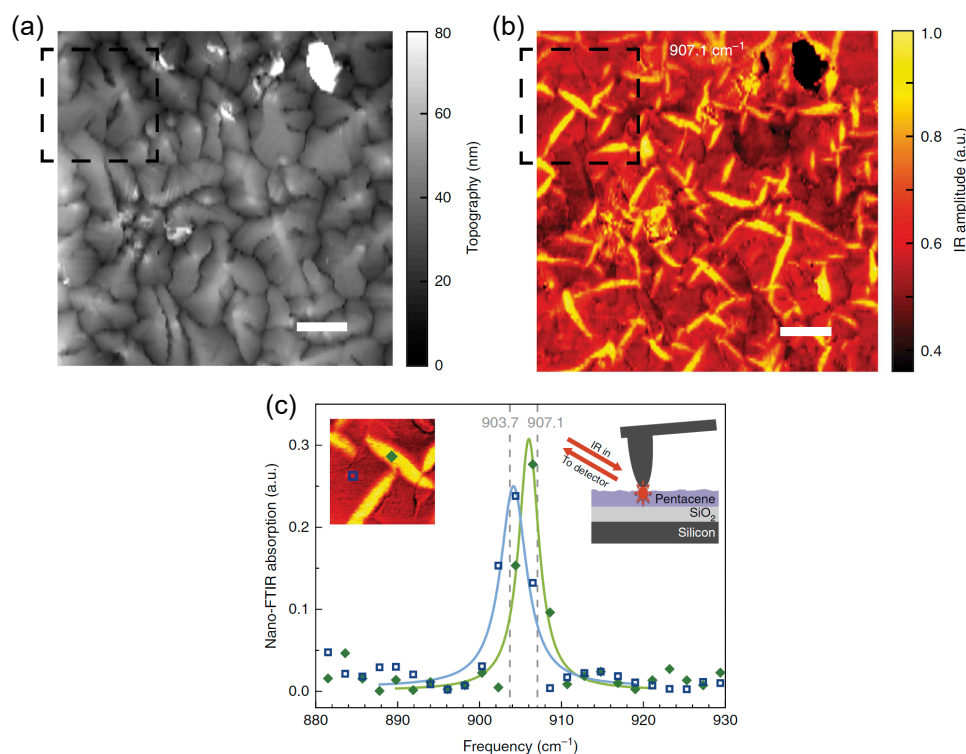


**Figure 4.** S-SNOM IR and FTIR images. (a) AFM topography of a pentacene thin film; (b) the corresponding IR-SNOM image excited with  $907\text{ cm}^{-1}$  wavelength light, scale bar is  $2\text{ }\mu\text{m}$ ; (c) Nano-FTIR spectra taken at two different locations representing the thin film and bulk phases of a pentacene film ( $40\text{-nm}$  thick) deposited on an  $\text{SiO}_2$  substrate. Lorentzian fits (curves) to the data reveal that the bulk phase (green line, yellow ellipsoids in the image) displays a higher resonance frequency than the surrounding thin film phase (blue line, red phase in the images). Reproduced with permission from [45], Copyright Nature communications, 2014.

## 5. Applications of 3D-SNOM

Two-dimensional mapping of nanostructured surfaces at the sub-wavelength limit has been slowly maturing for decades, and eventually led to many significant breakthroughs including tip design and coupling to other systems such as IR spectroscopy. 3D light mapping has by comparison not been as greatly utilized. Early work in this field employed aperture tips composed of tapered optical fibers to collect images at variable distances from the surface without the use of advanced AFM based force modulation [46,47]. In one case the researchers were able to detect Weiner fringes which are an interference pattern arising from interference between incident and reflected light [46]. It was found that the fringe pattern can be collected through the nanoscale aperture of an optical fiber, and can be used to reconstruct an image of the sample surface able to resolve features  $\sim 100\text{ nm}$  in size. Alternatively, images can be collected in a plane above a sample surface to image scattered light from nanostructures such as a microgratings [47]. This work demonstrated that SNOM can be used to map light scattering patterns arising from devices in three dimensions using a nano aperture tip.

These early studies lead to mapping of light and electric near-fields in three dimensions that can provide unique insight for device applications where the spatial structure of plasmonic and magnetic fields as well as forward scattered light fields can greatly affect device operation and performance. In the following section, applications of 3D SNOM compared to traditional 2D scanning are discussed, with examples of the use of 3D SNOM to study and improve the design of organic solar cells, nano-aperture antennas, nanoparticle arrays, and photonic crystal waveguides [28,29,34,48–52].

Figure 5 illustrates the equipment setup that can be used for 3D SNOM measurements. This method employs a variation of collection mode where illumination is directed from the substrate

side through an inverted microscope using a laser light source in the case transparent or nearly transparent samples [48]. Alternatively the sample may be illuminated from the surface side, but laser illumination from the backside of the substrate has been found to greatly reduce the background of scattered far-field light and improve the near-field signal intensity. A SNOM image in three dimensions can be generated using a SNOM tip mounted on an AFM system and scanned in the near-field of the sample surface at variable distances  $z$  away from the surface. The tip is raster scanned over the sample surface in the  $x$ - $y$  plane while moving at fixed intervals in the  $z$ -direction using a piezoelectric scanner. Light is detected through an upright confocal optical microscope focused on the aperture at the end of the tip for each point  $(x, y, z)$  in the scan. The intensity of scattered light collected by the tip aperture is transmitted via optical fiber to be measured by a photomultiplier tube. Using scans consisting of  $(x, y)$  slices in the  $z$  direction, the entire near-field and its boundary with the far-field can be mapped.

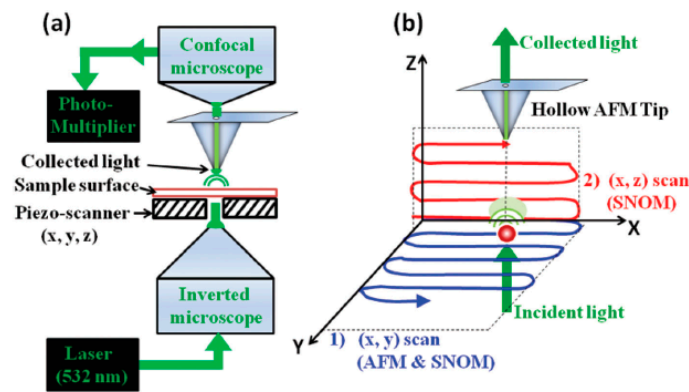


**Figure 5.** Schematic of collection mode operation 3D SNOM system. (a) The piezo-scanner is capable of moving the tip in  $x$ ,  $y$  and  $z$  directions to position the tip in any location in 3D space; (b) In the 3D SNOM configuration, SNOM and topography images can be simultaneously obtained from AFM/SNOM scans of the  $x$ - $y$  plane along the sample surface. Scanning along  $x$ - $z$  planes at a constant  $y$  can be used to obtain a cross-section of light scattered by nanostructures at different heights from the sample surface. Reproduced with permission from [48], Copyright Nanoscale, 2015.

The extent of the mapping capabilities depends on the specific arrangement of a given SNOM instrument. Table 1 below provides details of 3D SNOM microscope configurations that have been reported in the literature in terms of scanning range, type of tip, and illumination source used. From the table SNOM images can be collected over volumes that are hundreds of microns in size, with a variety of illumination sources ranging from infrared and visible light lasers to direct thermal heating of the tip and sample.

**Table 1.** Configuration of SNOM instruments reported in the literature.

Author	Year	Ref.	Microscope Configuration	$z$ -Axis Scanned	$x$ - $y$ Dimension ( $\mu\text{m}^2$ )	Illumination Wavelength
Umeda	1992	[46]	Bent metal, 100 nm aperture	30 $\mu\text{m}$	400	669 nm
Bacsa	2006	[47]	Optical fiber, 0.3 $\mu\text{m}$ aperture	2 $\mu\text{m}$	9	780 nm
Bek	2006	[13]	Various apertureless	9 $\mu\text{m}$	120	670 nm
Lalouat	2007	[37]	50 nm Cr-Au coated apertureless	50 nm	3	1.5 $\mu\text{m}$
Buresi	2009	[32]	Al coated, 100 nm aperture	fixed †	8	1.53 $\mu\text{m}$
Schnell	2010	[35]	Si apertureless	30 nm	1.3	9.3 $\mu\text{m}$
Olmon	2010	[53]	Pt coated 400 nm apertureless	200 nm	5 $\mu\text{m}$ line scan	10.6 $\mu\text{m}$
Guo	2010	[51]	Al coated 150 nm aperture	microns	1	457 nm
Huth	2011	[43]	FTIR, Au coated apertureless	fixed †	5 $\mu\text{m}$ line scan	10.7 $\mu\text{m}$
Jones	2012	[44]	FTIR, apertureless	10 $\mu\text{m}$	5	thermal heating *

Table 1. Cont.

Author	Year	Ref.	Microscope Configuration	z-Axis Scanned	x-y Dimension ( $\mu\text{m}^2$ )	Illumination Wavelength
Rotenberg	2012	[31]	100 nm aperture	fixed †	24	1.55 $\mu\text{m}$
Chen	2012	[38]	Apertureless	fixed †	4	9–10 $\mu\text{m}$
Bauld	2012	[54]	80 nm aperture	8 $\mu\text{m}$	50	532nm
Costantini	2012	[55]	Square hollow pyramid, 100 nm aperture	microns	32 $\mu\text{m}$ line scan	980 nm
Denkova	2013	[11]	Al coated pyramid, 100 nm aperture	30 nm	5	0.4–2 $\mu\text{m}$
Rotenberg	2013	[30]	100 nm aperture	fixed †	800	1.55 $\mu\text{m}$
Kihm	2013	[34]	100 nm aperture	10 $\mu\text{m}$	100	780 nm
Amenabar	2013	[42]	FTIR, Au coated apertureless	fixed †	1.2	4–14 $\mu\text{m}$
le Feber	2014	[29]	Al coated, 218 nm aperture	380 nm	1	1.57 $\mu\text{m}$
Denkova	2014	[33]	Al coated hollow pyramid, 90 nm aperture	fixed †	1	0.4–2 $\mu\text{m}$
Westermeier	2014	[45]	FTIR, apertureless	fixed †	180	907 nm
Liu	2014	[56]	Infrared, apertureless	0.4 $\mu\text{m}$	7.2	1.56 $\mu\text{m}$
Ouyang	2015	[28]	80 nm aperture	2 $\mu\text{m}$	4	532 nm
Ikeda	2015	[41]	20 nm apertureless	150 nm	1.5	633 nm
Ezugwu	2015	[48]	80 nm aperture	2 $\mu\text{m}$	2.5	532nm
Li	2015	[50]	Si 10 nm apertureless	100 nm	0.15	633 nm
Martinez-Marrades	2016	[49]	Square -based pyramid, 100 nm aperture	2.7 $\mu\text{m}$	3.6 $\mu\text{m}$ line scan	660 nm
Bulat	2016	[57]	Optical fiber, 50 $\mu\text{m}$ aperture	fixed †	1600	532 nm
Klein	2017	[58]	Au coated, 150 nm aperture	2 $\mu\text{m}$	10	663 nm

\* Thermal heating of probe and stage. † Scans in the z-x or z-y planes were not performed.

### 5.1. 3D Probing of Near-Fields of Nanostructures

Surfaces composed entirely of metallic nanoparticles or composite films embedded with nanoparticles may be incorporated in the architectures of optoelectronic devices to optimize their performance. Nanoparticles can impart increased efficiency or functionality to traditional device architectures if their implementation is well understood. 3D SNOM has been demonstrated to represent an outstanding tool for a deeper understanding of similar systems, whereas other scanning probe techniques are surface-sensitive only. Figure 6 summarizes the use of 3D SNOM to map plasmonic waves and electric field enhancement. Gold nanoparticles embedded in a polyimide thin film were investigated using SNOM equipped with an 80 nm aperture tip with illumination provided by 532 nm laser light (Figure 6e) [54]. Gold nanoparticles are promising for use in nanoplasmonic devices because they are strongly resistant to environmental oxidation, while displaying an appropriate plasmon resonance suitable for harvesting light in the visible range. Gold nanoparticles nucleated within the film layer with different annealing temperatures and atmospheres were visible in simultaneous AFM (left side of Figure 6a–d) and c-SNOM (right side of the same) images. Comparison of AFM and c-SNOM images for these transparent samples qualitatively indicates the different depth of various nanoparticles within the film as on the surface detectable by AFM or below the surface only detectable by SNOM. AFM indicates large (up to 2  $\mu\text{m}$ ) metallic microclusters near the surface of the films, while smaller (<500 nm) nanoparticles are observed much deeper below the surface. 3D SNOM imaging scanning pattern in Figure 6e is used to image the plasmonic waves and electric field enhancement at a distance z above the surface (Figure 6f). The mapping shows enhanced light scattering intensity close to the surface of the films, with areas of constructive and destructive interference evident moving away from the sample surface up to a distance of several microns.

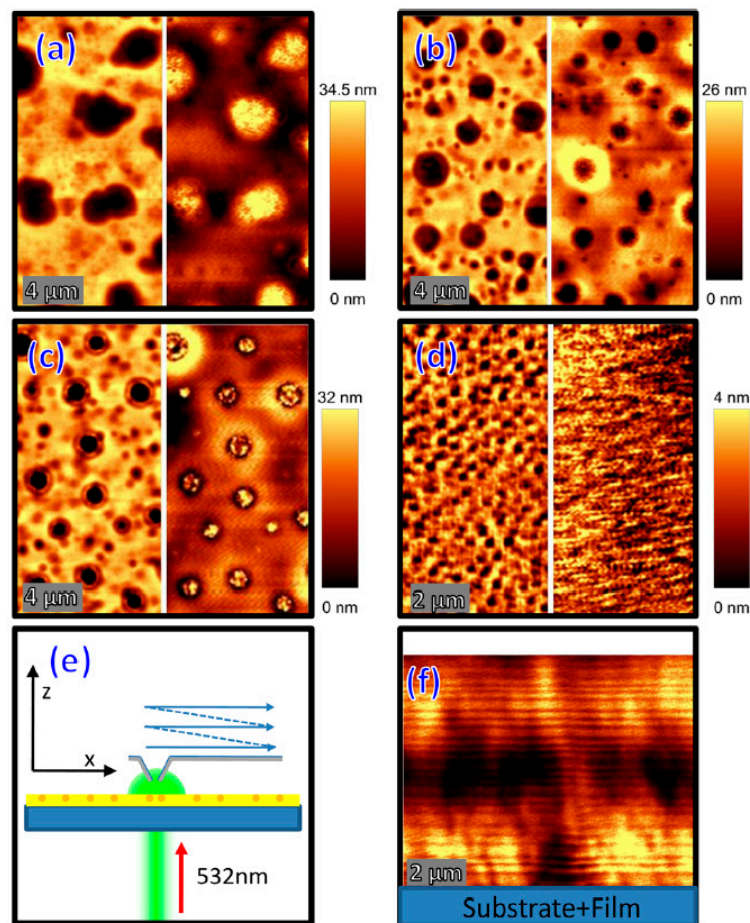


**Figure 6.** AFM (left) and SNOM (right) images of Au nanoparticles embedded in polyimide. (a) Annealing at 150 °C in an oxygen deficient environment creates large micron sized particles. Identical samples annealed at (b) 250 °C; and (c) 450 °C show a decrease in nanoparticle size as the temperature is increased; (d) Annealing under atmospheric conditions at 250 °C shows significantly different morphology consisting of smaller particles 250 nm in size; (e) Schematic of z-x c-SNOM scans using an inverted configuration with laser illumination from beneath the substrate; (f) Near-field light recorded moving away from the sample surface. Reproduced with permission from [54], Copyright Applied Physics Letters, 2012.

In addition to gold nanostructures, semi continuous films of copper nanoparticles have also been identified as components for optoelectronic devices to manipulate scattered light fields and were studied by multidimensional SNOM methods. Small metallic particles of appropriate shape and size can be used to generate large plasmonic field enhancements that may be useful for optoelectronic devices [59]. 3D spatial mapping of these nanoparticles in the near-field revealed new phenomena concerning light scattering by nano-objects. Radiation scattering from nanostructures may have several potential applications in optoelectronic devices: in addition to providing information about the size, shape, and location of nanoparticles in a film, 3D SNOM can be used to map scattered light fields in space. The properties, location, and intensity of scattered light fields are of paramount importance for controlling light scattering in optoelectronic devices such as solar cells, waveguides, and light emitting diodes. 3D SNOM can be used to map constructive and destructive interference of scattered light fields to help improve the design or optimize the efficiency of such devices.

Figure 7 illustrates how 3D SNOM mapping could be combined with AFM to image arrays of thermally nucleated copper nanoparticles obtained using an aperture tip [48]. The AFM image in shown in panel (a) was collected simultaneously with the SNOM image shown in panel (b) Yellow

pixels in panel (b) represent the location of nanoparticles in panel (a) and show regions near the nanoparticles of higher intensity forward-scattered light. Comparing the background signal to that of the copper nanoparticles clearly indicates that very near the sample surface ( $z \approx 0$ ), the intensity of light scattered by the bare glass substrate is significantly lower in intensity compared to light scattered from the nanoparticles. From the AFM image the nanoparticle size is significantly smaller than the illumination wavelength,  $\lambda = 532 \text{ nm}$ , which means the scattered electric field produced by the nanoparticles is better represented as an infinite superposition of multipoles rather than a purely dipole field [48]. Such a multipolar field is expected to undergo a series of intensity oscillations moving away from the surface showing bands of maxima and minima interval distances  $z$ , a property that is not displayed by a purely dipole field [60].

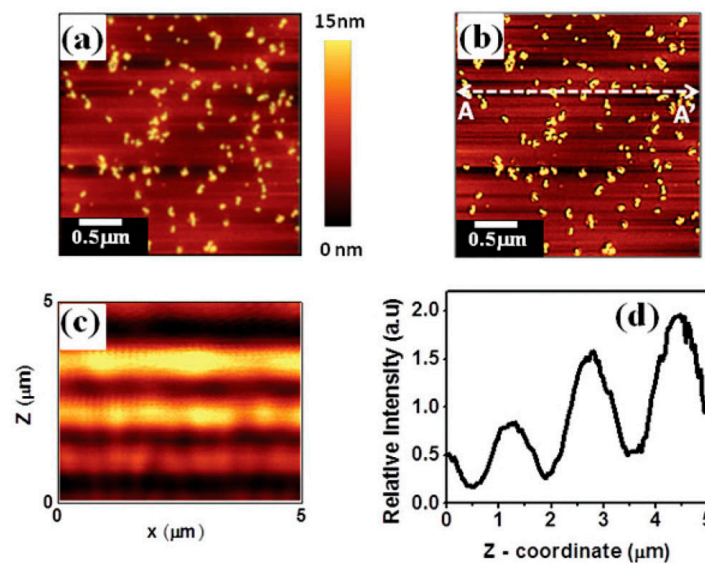


**Figure 7.** (a) Topographic AFM and (b) c-SNOM images obtained simultaneously; (c) Light intensity mapping ( $x, z$ ) measured along the A–A' cross-section in panel (b,d) the integrated intensity profile in the  $z$ -direction along the A–A' cross-section showing the positions of constructive (maxima) and destructive (minima) interference of forward light scattered from Cu-nanoparticles in panel (c). Reproduced with permission from [48], Copyright Nanoscale, 2015.

These oscillations are visible (Figure 7c) in an ( $x, z$ ) c-SNOM scan of the line A–A' shown in Figure 7b, confirming the multipolar nature of the near-field. The bands of oscillating intensity are found to extend into the far-field up to distances of  $5 \mu\text{m}$  away from the surface, and possess a nearly uniform intensity along the  $x$ -direction excepting a relatively lower intensity corresponding to the largest particles. This effect is observed because even on a surface where the nanoparticles are not closely packed, they cannot be considered to be isolated when the inter-particle distances remain smaller than the wavelength of probing light. Variations in particle diameter were found to affect the intensity of the first maximum of forward-scattered light as a function of average particle size. Light scattered from nanoparticles with larger diameters is coupled more closely to the surface, which is attributed to the dependence of the cross-section for near-field light absorption and scattering on the particle size [59]. As a consequence of this copper nanoparticles with a diameters of  $80 \text{ nm}$  or greater exhibit multipolar effects induced by Mie scattering that causes strong coupling of this scattered light to the substrate in the nanoparticle vicinity.

Figure 7d presents the integrated intensity of light scattered along the A–A' cross-section labeled in Figure 7b and corresponding to the  $z$ -axis of Figure 7c. Maxima and minima arising from constructive and destructive interference, respectively, are visible on the micron scale moving away from the surface. For the nanoparticles specific to this sample the first intensity maximum of forward-scattered light is

observed 1200 nm above the surface, within the far-field of scattered light. The absolute maxima occurs further away in the far-field at  $\Delta z = 4400$  nm. This information can be used to achieve efficient light harvesting in devices such as solar cells by incorporating a layer of nanoparticles into their architecture at the appropriate location.

A variation of 3D SNOM utilized stroboscopic measurements of different faces of the same film. This technique has been used to great effect to study symmetry breaking induced by IR laser illumination in a vanadium dioxide ( $\text{VO}_2$ ), thin film using IR s-SNOM. In strongly correlated electron materials, broken symmetries can result in separation of multiple phases in the course of a solid-solid phase transition, where  $\text{VO}_2$  exhibits such a phase transition at a temperature close to room temperature (340 K) [56]. Figure 8 shows s-SNOM near-field images using an 18.8 mW near-IR pump laser taken at three different locations across the surface of a 250 nm  $\text{VO}_2$  film surface with their corresponding AFM images. Elevating the sample temperature to 334 K induces a highly oriented stripe state that presents a herringbone pattern with two distinct orientations representing the two equivalent in-plane orientations of the monoclinic  $c$ -axis [56].

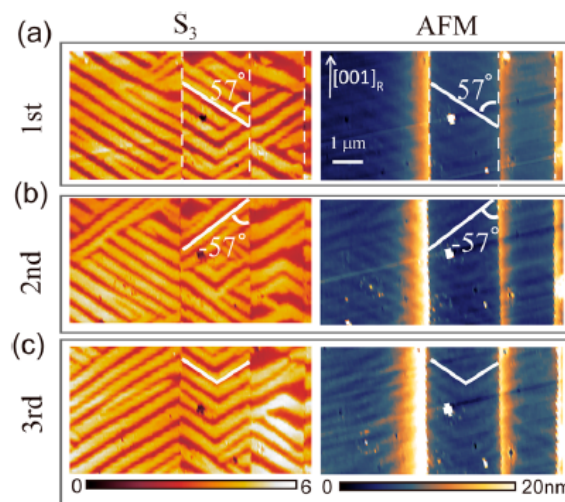


**Figure 8.** AFM and SNOM images of a  $\text{VO}_2$  film undergoing 18.8 mW pump laser induced strain. The left side of (a–c) show SNOM ( $S_3$ ) images with AFM images on the right. The pump laser was switched off for 1 s between each scan. After each switch, patterns are formed due to a spontaneous structural symmetry breaking, with stripes aligning along two possible orientations of the monoclinic  $c$ -axis shown by white lines. Reproduced with permission from [56], Copyright Applied Physics Letters, 2014.

These images are indicative of a spontaneous symmetry-breaking phase separation due to the blocking of the pump laser between measurements that varies the temperature of the sample. The re-illumination at that start of each scan produces a new strained architecture in the film that is similar but uniquely different from the previous state, and can be seen in both s-SNOM and AFM images. The symmetry breaking in this film can be understood considering a Landau-like free elastic energy model; as the material goes through a transition to a distorted phase of lower symmetry, long-range elastic modes couple to allowed short-range modes to yield two energy minima with equal potentials and mirror symmetry, corresponding in this case to two different monoclinic  $c$ -axis orientations with mirror symmetry [56].

To gain additional insight into the structure of the films after a phase transition, s-SNOM measurements were also conducted in the cross-sectional face of the  $\text{VO}_2$  film, as shown in Figure 9. These measurements were collected at a temperature 5 degrees below the transition temperature, to produce three adjacent regions are shown with characteristic near-field patterns. These images can be used to map the metal nucleation by the property that a larger s-SNOM intensity corresponds to a

higher IR conductivity a greater metal density [56]. Although the nucleation pattern varies somewhat across the film, within all the cross-section regions metallic nucleation occurs preferentially at the film/substrate interface where the epitaxial strain is the strongest. These metallic regions can then extend up to the VO<sub>2</sub> film surface, where a stripe like herringbone pattern emerges seen in Figure 8. Both cross-sectional and planar s-SNOM mapping enables a nanoscopic investigation of spontaneous symmetry breaking in a 3D geometry. This type of analysis can be extended to other materials, and illustrates a complimentary use of 3D SNOM to scan multiple faces of the same material.

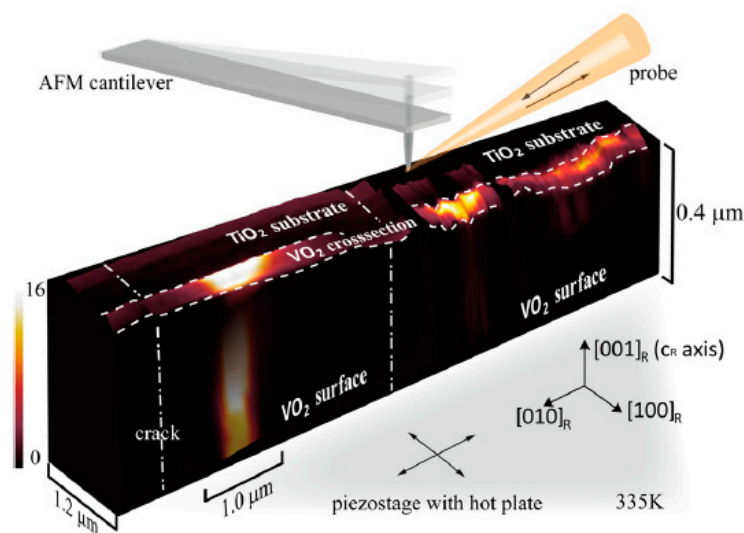


**Figure 9.** IR s-SNOM image of the cross-section of the VO<sub>2</sub> film at 335 K. The white lines represent the boundary between crystal domains as seen in Figure 8. The cross section shows 3 distinct regions, which indicate the nucleation of metal atoms where a more intense IR s-SNOM signal corresponds to a higher IR conductivity. The image indicates that metal nucleation happens preferentially at the film/substrate interface where the epitaxial strain is strongest. Reproduced with permission from [56], Copyright Applied Physics Letters, 2014.

## 5.2. Optimization of Nano-Optical Devices

The first use of 3D SNOM to probe a scattered light field of an optoelectronic device was accomplished by means of a focusing waveguide grating coupler (FWGC) as an experimental system [61]. This study was undertaken to evaluate SNOM as a complimentary tool to characterize FWGCs, which normally are difficult and time consuming to accurately analyze, requiring a full 3D calculation to predict their waveguiding properties. The focal spot produced by such FWGCs is nanoscale in size near the grating surface, and therefore can only be imaged using non-diffraction limited techniques. In this case, SNOM was capable of imaging the real performance of the FWGC by imaging the spot at different heights about the sample, for comparison to a much simpler 2D Bloch wave analysis which was able to fully characterize the FWGC [61]. This initial investigation showed the utility of 3D SNOM beyond scanning the near-field very close to the surface, and how it can be used to study light scattering antennas and waveguides.

3D-SNOM has since been used to investigate resonant illumination of nano antennae consisting of ordered nano-holes as shown in Figure 10a [49,55]. Nano hole antennas can possess interesting optoelectronic properties used to scatter light in a controlled way. The nano hole antenna shown in Figure 10a consists of a 40 nm thick gold film perforated with 17 holes of 150 nm in diameter arrayed in a line separated by 20 nm spaces and illuminated with 660 nm laser light [49]. Panel (b) shows the result of a 2D digital heterodyne holography scan above the sample surface to image scattered light. Although DHH is capable of 3D imaging similar to 3D SNOM, it is a far-field technique and therefore the resulting image is diffraction limited. This can be seen from the corresponding

SNOM image showing much higher resolution details of the nano holes. This nanostructure has also been investigated in three dimensions to probe the light scattered above the nanoholes as shown in Figure 10c. The uniform light intensity near the surface indicates coupling between the nano holes. The interference pattern observed in the SNOM image is a consequence of light originating from the surface that is back scattered from the tip itself and reflected from the Au surface to be collected by the tip.

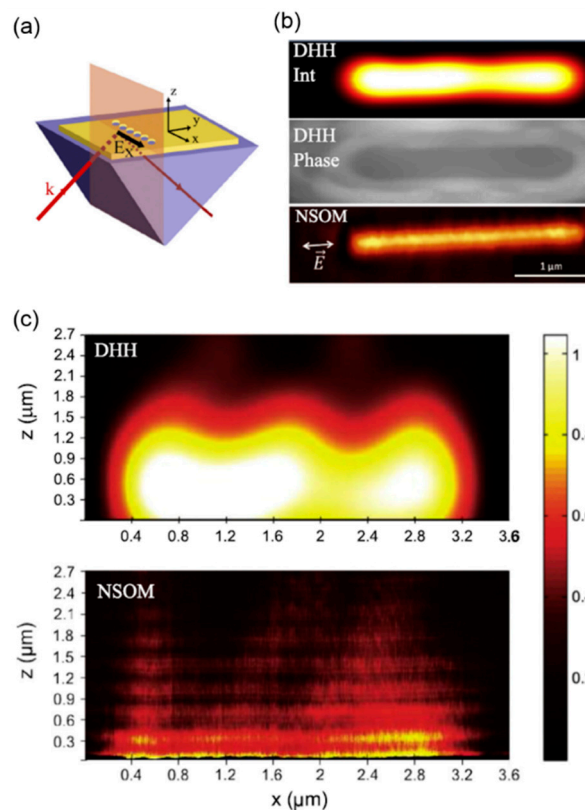


**Figure 10.** Resonant illumination of nano hole antenna. (a) Nano hole antenna experimental configuration; (b) 2D scan of the nano hole surface using far-field DHH imaging and phase as well as c-SNOM; (c) Scattered light intensity in a plane perpendicular to the sample surface. Reproduced with permission from [49], Copyright Optics Communications, 2016.

Nano antennas or apertures with more exotic shapes such as the bowtie antenna [50,51] have been sought after for their light scattering properties. Bowtie shaped antennas are designed to produce enhanced electric fields in the aperture between the two bowtie halves. Figure 11 shows the optical amplitude distribution in the space above a bowtie antenna of this type, using s-SNOM imaging. This bowtie antenna was manufactured using focused ion beam milling to produce an aperture with an outline of 150 nm and a gap size of 20 nm in a 60 nm gold film to [50]. From Figure 11a, the electric ( $E_z$ ) field is concentrated along the edges of the bowtie-shaped aperture gap. The curvature of the side walls of the bowtie aperture gap allows the near-field to spread along the curvatures and reduce its spatial confinement to the aperture. From the 3D SNOM scans the near-field can be seen to extend up to 20 nm from the film surface, at which point it drops off sharply in intensity. The optical phase image (Figure 11b) clearly identifies a  $180^\circ$  phase shift that is characteristic of bowtie apertures, and extends past the near-field boundary seen in the amplitude image [50,51].

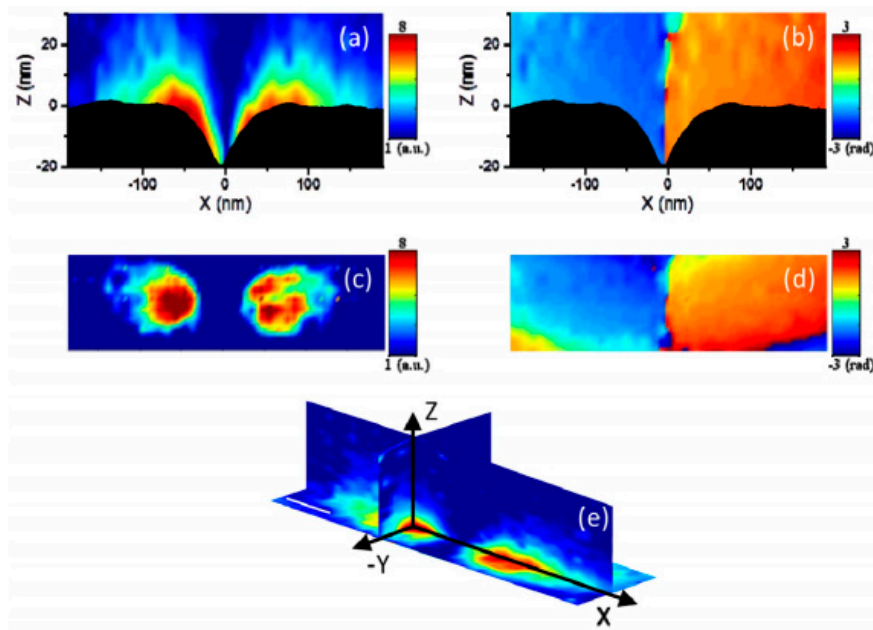


**Figure 11.** 3D SNOM amplitude and phase images of a bowtie antenna. The amplitude (a) and phase (b) images in an  $x$ - $z$  plane showing a cross-section of the bowtie aperture. Panels (c) and (d) are 2D amplitude and phase images, respectively, sized  $400 \text{ nm} \times 100 \text{ nm}$  and taken at the bowtie antenna surface,  $z = 0$ ; (e) Combined scans showing the 3D light field of the antenna where the white scale bar represents 50 nm. Reproduced with permission from [50], Copyright Optics Express, 2015.

The 2D optical amplitude and phase in an  $x$ - $y$  plane directly above the film surface corresponding to  $z = 0$  are constructed from the volume data and shown in Figure 11c,d. In Figure 11c, two separate hot spots of the  $E_z$  field with FWHMs of 90 nm are clearly identified above the apex of each half of the bowtie, with a minima in the field at the center corresponding to the gap of the bowtie aperture. The phase shift seen in the  $x$ - $z$  scan is reproduced at the bowtie antenna surface, showing that this effect extends spatially in three dimensions. The full three-dimensional field can be reconstructed from these scans; Figure 11e shows the intersection of the  $x$ - $y$ ,  $x$ - $z$ , and  $y$ - $z$  data planes.

In addition to nano antennae, photonic crystal waveguides (PhCWs) possess evanescent wave fields that have been investigated in great detail using SNOM imaging. In these devices, 3D SNOM can be utilized to examine the six components of the electric and magnetic fields. Measurements at increasing distances  $z$  above the crystal can be used to differentiate between parallel electric ( $E_{\parallel}$ ) and magnetic ( $H_{\parallel}$ ) fields. In the  $x$ ,  $y$  plane of symmetry, only transverse components ( $E_x$ ,  $E_y$ ,  $H_z$ ) of the electromagnetic field are non-zero and have been detected using SNOM [29]. However, as the distance from the surface increases the relative amplitudes of the electric and magnetic fields and their spatial profiles changes. This divergence occurs because a given mode is composed of many Bloch harmonics in superposition, each of which experiences a different decay in the  $z$ -direction, which can be investigated using 3D SNOM.

Figure 12 shows the result of 3D SNOM investigations of a silicon PhCW with 120 nm radius holes separated by 420 nm spaces. This structure is illuminated by 1570 nm light along the plane of the waveguide, which is maintained in the waveguide by the photonic bandgap of the surrounding holes, and confined to the bulk of the silicon by total internal reflection. The PhCW acts a waveguide to confine light incident on the edge of the silicon PhCW between two rows of periodic holes that create a periodicity in the dielectric properties of the silicon resulting in confinement of the light between the holes. Each individual small panel in Figure 12 is a 2D scan of a portion of the waveguide, collected at a height above the surface given by the scale on the left of the figure. Panels (c) and (d) of Figure 12 show the measured light field above the sample where  $L_x$  and  $L_y$  represent separate detectors that are set to

preferentially measure the  $E_x$  or  $E_y$  field components respectively. The  $L_x$  signal presents a minimum along the center of the waveguide (arrow at the bottom of panel c) that is similar to the calculated  $E_x$  in panel a as expected. However, the signal obtained from  $L_y$  greatly resembles the calculated  $H_x$  field rather than  $E_y$  as expected. These observations indicate that the 3D SNOM measurements above the sample surface actually measure a superposition of the  $E_{\parallel}$  and  $H_{\parallel}$  fields. Therefore, using a symmetrical c-SNOM probe it is possible to access all components of the electromagnetic spectrum above a PhCW using 3D SNOM mapping. The individual components can be further decoupled using Maxwell's equations combined with additional constraints such as symmetry in the sample or measurements with probes of different shapes [29].

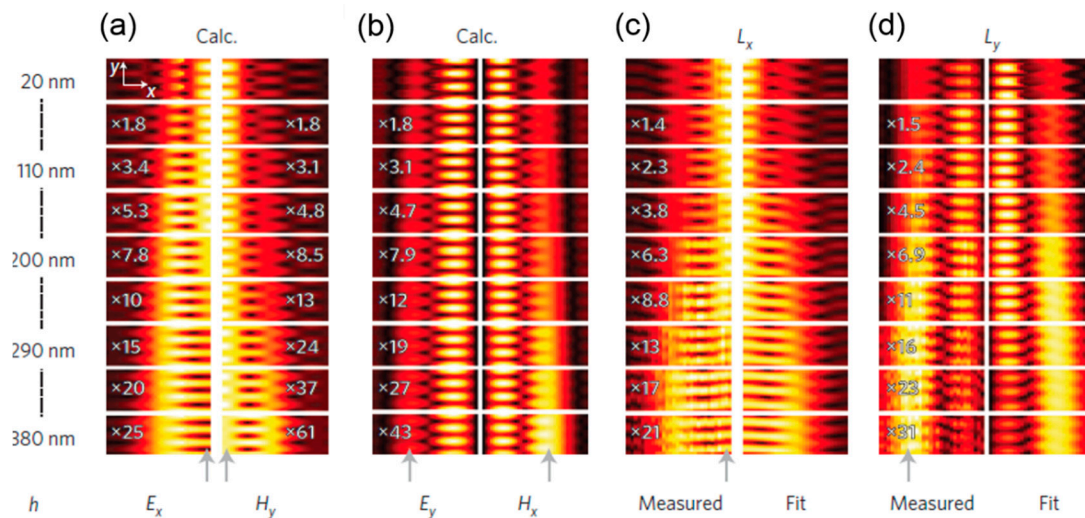


**Figure 12.** 3D SNOM detection of E and H fields simultaneously. (a,b) Calculated electric and magnetic fields in  $x$ - $y$  planes above the PhCW surface up to a distance of 380 nm. (c,d) Measured 3D SNOM data (left) and data fitted to the calculated result (right).  $L_x$  and  $L_y$  represent two photodetectors arranged to preferentially detect  $E_x$  and  $E_y$  fields, respectively. Reproduced with permission from [29], Copyright Nature Photonics, 2014.

Beyond the study of previously existing waveguide architectures, 3D SNOM has also been used to aid in the design of other types of devices such as organic bulk heterojunction (BHJ) solar cells. The distribution of scattered light resulting from a nanostructured surface can also be utilized to enhance the performance of BHJs. The prospects of this concept have been explored using a structured plasmonic architecture solar cell containing a layer of copper nanoparticles. The architecture is shown in Figure 13c,e where an  $\text{SiO}_2$  thin film is placed as a spacer between the solar cell active layer and a layer of copper nanoparticles [48]. Figure 13a illustrates the integrated scattered light intensity in the  $\text{SiO}_2$  modified device compared to a reference cell. A region of forward-scattered light exhibiting constructive interference is revealed from  $z = 0$ –550 nm above the nanoparticle layer when the spacer is present, as well as strong constructive interference at a greater distance from the nanoparticle layers. This enhancement region is the result of coupling between normally incident plane waves on the  $\text{SiO}_2$  surface and waves travelling laterally, parallel to the surface. The superposition of these lateral and normal components leads to scattered light with increased intensity that is combined with the normally incident light in constructive interference. By contrast, when the spacer is not used destructive interference is observed in a band 160 nm from the sample surface. This has the effect of considerably depleting the near-field in the region where the solar cell active layer would be placed in a typical architecture. In the spacer-enhanced cell the amplified forward-scattering field is ideally located to fall in the active solar cell region.

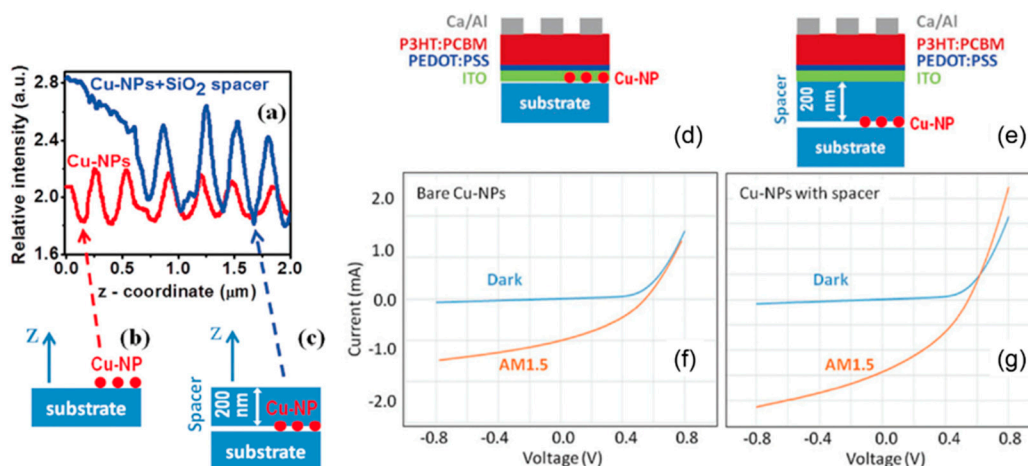


**Figure 13.** Intensity profiles of scattered light above the copper nanoparticles are shown in panel (a) for two cases of (b) bare nanoparticles and (c) nanoparticles modified with an SiO<sub>2</sub> spacer. Intensity enhancement of scattered light is observed when the spacer is in place. These films are subsequently incorporated into solar cell architectures of (d) the reference solar cell containing bare copper nanoparticles without a spacer and (e) the enhanced cell including a 200 nm SiO<sub>2</sub> spacer. I–V characteristics of the solar cells with a Cu-nanoparticle plasmonic layer (f) without and (g) with the SiO<sub>2</sub> spacer between copper nanoparticles and the ITO–P3HT/PCBM solar cell active layer. Reproduced with permission from [48], Copyright Nanoscale, 2015.

The use of nanoparticle layers to enhance light collection was examined in solar cells fabricated with and without a SiO<sub>2</sub> spacer. Solar cell architectures of this type are shown schematically in Figure 13d,e consisting of a BHJ active layer prepared from a mixture of regioregular poly-(3-hexylthiophene-2,5-diyl) (P3HT) and [6,6]-phenyl-C<sub>61</sub>-butyric acid methyl ester (PCBM) [48]. A layer of copper nanoparticles is incorporated on top of the indium tin oxide electrodes in both devices to serve as a forward scattering layer, and I–V curves were collected under inert nitrogen atmosphere as shown in Figure 13f,g for the reference and spacer-enhanced solar cells, respectively. Although the I–V characteristics of the two devices are very similar under no illumination, a significantly larger photocurrent was extracted from devices containing the spacer, more than twice the value obtainable in the unmodified reference cell. The increase in photocurrent alone is sufficient to improve the power conversion efficiency (PCE) from  $\eta = 1.38\%$  with no spacer present to  $\eta = 3.08\%$  on average with the spacer. The increased PCE is a result of increased intensity of light scattered by the layer of copper nanoparticles into the active layer of the solar cell.

The light scattering properties of copper nanoparticles have also been extended to evanescent waveguide technology. It has been shown recently that arrays of copper nanoparticles can be thermally nucleated from a thin layer of copper deposited on few layer graphene sheets [28]. Under controlled conditions of annealing temperature and atmosphere, the nanoparticles can be encouraged to form ordered arrays with interesting optoelectronic properties [28]. Figure 14 presents scanning electron microscopy (SEM) images of copper nanoparticle arrays nucleated on graphene flakes at different annealing temperatures. Superlattices of copper nanoparticles are found to be formed at intermediate annealing temperatures ( $\sim 350$  °C) where nanoparticles nucleate preferentially along graphene armchair edges. At the extremes, nucleation is either limited by low temperature, or promotes the appearance of disordered arrays at higher temperatures.

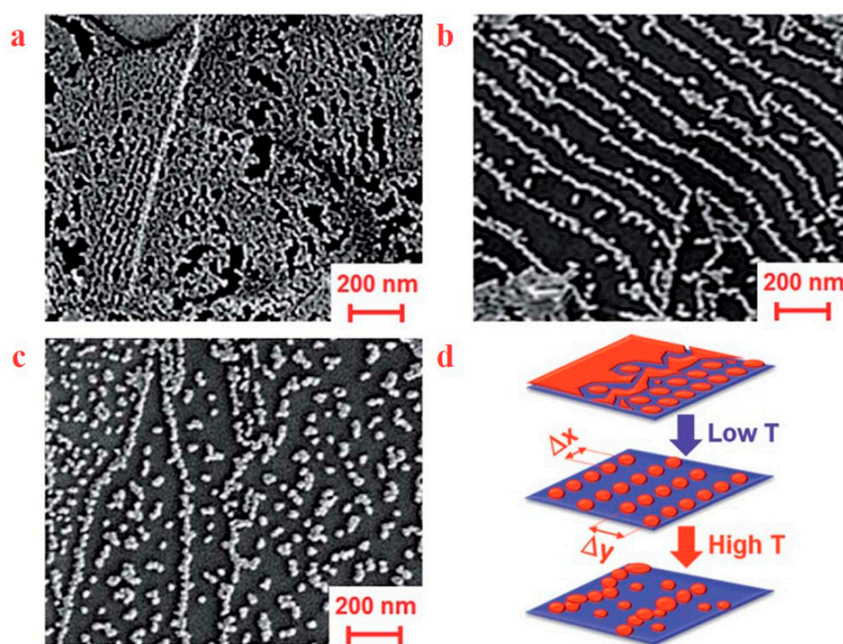


**Figure 14.** SEM images of copper nanoparticle decorated graphene thin films annealed for 8 h at (a) 200 °C (b) 360 °C, (c) 440 °C. (d) At lower temperatures copper nanoparticles are formed in an uneven layer, which are formed which transitions to assemblies of particles that become spatially separated at the highest temperature. Superlattices formed of lines of nanoparticles are formed at the intermediate temperature of 360 °C. Reproduced with permission from [28], Copyright RSC Advances, 2015.

C-SNOM ( $x, z$ ) scans were used to characterize the copper nanoparticle arrays and determine the electric field intensity perpendicular to the plane of the substrate during excitation by a laser source. Figure 15f,g schematically show how the laser light is applied to the copper nanoparticle superlattices, where an ordered lattice can exhibit waveguiding properties. Modes are generated by the laser source, with an evanescent near-field propagating along the sample surface which can be collected through the SNOM tip aperture.

Figure 15a–c show the AFM, c-SNOM, and SEM images, respectively, of the same copper nanoparticle super lattice. Figure 15d shows c-SNOM scans in  $z$ -direction for the two line sections, A–A' and B–B' representing superlattice and disordered areas. The light fields displayed indicate that section A–A' demonstrates evanescent waveguiding properties by the strong intensity observed near the surface with an absence of destructive interference. Another scan along the section B–B' with disordered nanoparticles exhibits the expected intensity oscillation along the  $z$ -axis that indicates incoherent Mie scattering from randomly arrayed nanoparticles [60].

The integrated light intensity profiles extracted from Figure 15d are shown in panel e relative to the distance away from the surface,  $z$ . Figure 15e shows an exponential decay of light intensity is observed in the proximity of ordered nanoparticle arrays (region A–A') moving away from the surface, in agreement with the evanescent wave decay profile. By contrast the scattered light intensity from the disordered section B–B' shows multiple oscillations. This effect arises from a superposition of multipole and incoherent Mie scattering [60].

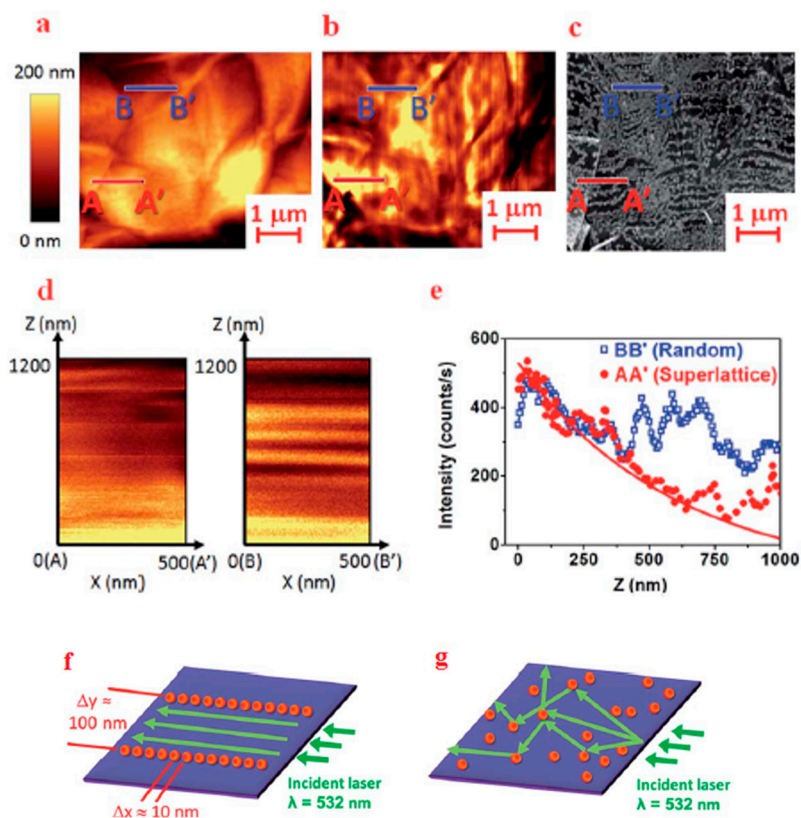


**Figure 15.** (a) AFM, (b) c-SNOM, and (c) SEM images obtained for the same area of a copper nanoparticle superlattice; (d) c-SNOM scans in the z-direction for cross sections A–A' and B–B' in panels a–c; (e) The integrated intensity shown in panel d identifies the exponential decay of the evanescent wave moving away from the surface along the region A–A' representing an ordered superlattice. Random interference patterns are observed for the randomly disordered area B–B'; (f) Light scattering within the superlattices is coherent as the periodic nanoparticles act as a waveguide; (g) Randomly distributed nanoparticles result in incoherent scattering and light absorption. Reproduced with permission from [28], Copyright RSC Advances, 2015.

The underlying mechanism of the copper nanoparticle array waveguide begins with laser light incident on the graphene at grazing incidence. In this case, the presence of the graphene layer determines the polarization of the propagating light. Graphene is an optically anisotropic material where the dielectric constant possesses a large in-plane imaginary part, while the out-of-plane imaginary part is very close to zero [62]. The result is that for light propagating a grazing incidence to the graphene edge, the in plane polarization component becomes strongly attenuated, while the out-of-plane component will continue to propagate along the graphene surface without significant attenuation. The nanoparticle superlattice offers a preferential direction for light propagation compared to unmodified graphene, corresponding to the direction of parallel lines of copper nanoparticles.

## 6. Conclusions

In conclusion, our review shows that advanced SNOM is a powerful imaging technique with immense potential that has so been only partially realized. With the advent of advanced nanofabrication methods, it is now possible to produce designer c-SNOM tips of varied composition with finely controlled aperture sizes from 100 nm to as small as 20 nm. Studies have shown that SNOM is able to map the complete electromagnetic near-field of nanostructures, even without resorting to specialized tip designs. Access to this unique near-field information has significant potential to improve the design and performance of optoelectronic devices. Imaging near-fields in three dimensions is a

natural extension on traditional 2D c-SNOM mapping to examine nanostructures, complementing the already robust list of complimentary techniques available including Raman, FTIR, and electromagnetic field imaging.

Nanoparticles and nanostructures have the potential to revolutionize device architecture and design by imparting new functionality to already established technologies. 3D SNOM is positioned to encourage this revolution by providing the capability to fully characterize scattered and near-field light from nanoparticles and nanostructures, and exploit them to improve device properties. Examination of the near-field of metal nanoparticles using 3D SNOM has been used to enhance the performance of organic BHJ solar cells through an increased understanding on the forward scattered light field. Efficient control of scattered light in solar cells enabled by 3D SNOM could lead to increased PCE without significant changes to existing solar cell architectures. 3D SNOM has also been shown to have the capability of mapping all components of electric and magnetic fields above PhCW structures using standard circular aperture tips.

3D SNOM is also not limited to mapping of light and electromagnetic near-fields. The sub wavelength resolution of SNOM can be combined with other techniques not covered in this article—such as thermoreflectance—to enhance the resolution beyond the diffraction limit and obtain the nanoscale thermal conductivity. Synergy with an AFM system also allows SNOM to be easily coupled with other nanoscale force microscopies such as Kelvin probe force microscopy or conducting probe AFM. Multiple SNOM systems can be coupled together to simultaneously inject and collect light from nanostructures [58]. Time resolved studies are also possible with switching or chopping of external light sources to examine temporal properties of nanostructured surfaces. Modifications to AFM More exotic modifications can be considered. SNOM has been shown to be well suited for investigation of biological systems where non-destructive and contactless methods are in high demand for nanoscale imaging of live cells [57]. 3D SNOM is envisaged to lead to breakthroughs in the study of biological systems with nanoscale imaging of live cells, as well as improved design and operation of nanoscale light management devices. 3D SNOM is well positioned to augment the study of nanoscale properties of materials, with a bright future ahead for sub-wavelength resolution imaging.

**Acknowledgments:** P.B. acknowledges a MITACS Accelerate Postdoctoral Fellowship. G.F. acknowledges a Canada Research Chair in carbon-based nanomaterials and Nano-optoelectronics. The authors would like to thank Teeno Ouyang, Jaewoo Park and Reg J. Bauld for some of the experiments that led to the results discussed here, and for fruitful discussions. Funding from the Canada Foundation for Innovation (grant No. 212442) and the Discovery Grant program of the Natural Sciences and Engineering Research Council of Canada (RGPIN-2015-06004) are also gratefully acknowledged.

**Conflicts of Interest:** The authors declare no conflict of interest.

## References

1. Weisenburger, S.; Sandoghdar, V. Light microscopy: An ongoing contemporary revolution. *Contemp. Phys.* **2015**, *56*, 123–143. [[CrossRef](#)]
2. Hell, S.W. Toward fluorescence nanoscopy. *Nat. Biotechnol.* **2003**, *21*, 1347–1355. [[CrossRef](#)] [[PubMed](#)]
3. Sarunic, M.V.; Weinberg, S.; Izatt, J.A. Full-field swept-source phase microscopy. *Opt. Lett.* **2006**, *31*, 1462–1464. [[CrossRef](#)] [[PubMed](#)]
4. Dubois, A.; Vabre, L.; Boccara, A.-C.; Beaufort, E. High-resolution full-field optical coherence tomography with a Linnik microscope. *Appl. Opt.* **2002**, *41*, 805–812. [[CrossRef](#)] [[PubMed](#)]
5. Shirazi, M.F.; Kim, P.; Jeon, M.; Kim, J. Full-field optical coherence tomography using galvo filter-based wavelength swept laser. *Sensors* **2016**, *16*, 1933. [[CrossRef](#)] [[PubMed](#)]
6. Huang, B.; Wang, W.; Bates, M.; Zhuang, X. Three-dimensional super-resolution imaging by stochastic optical reconstruction microscopy. *Science* **2008**, *319*, 810–813. [[CrossRef](#)] [[PubMed](#)]
7. Huang, B.; Jones, S.A.; Brandenburg, B.; Zhuang, X. Whole-cell 3D STORM reveals interactions between cellular structures with nanometer-scale resolution. *Nat. Methods* **2008**, *5*, 1047–1052. [[CrossRef](#)] [[PubMed](#)]
8. Rotenberg, N.; Kuipers, L. Mapping nanoscale light fields. *Nat. Photonics* **2014**, *8*, 919–926. [[CrossRef](#)]

9. Neumann, L.; Pang, Y.; Houyou, A.; Juan, M.L.; Gordon, R.; van Hulst, N.F. Extraordinary optical transmission brightens near-field fiber probe. *Nano Lett.* **2011**, *11*, 355–360. [[CrossRef](#)] [[PubMed](#)]
10. Ogletree, D.F.; Schuck, P.J.; Weber-Bargioni, A.F.; Borys, N.J.; Aloni, S.; Bao, W.; Barja, S.; Lee, J.; Melli, M.; Munechika, K.; et al. Revealing optical properties of reduced-dimensionality materials at relevant length scales. *Adv. Mater.* **2015**, *27*, 5693–5719. [[CrossRef](#)] [[PubMed](#)]
11. Denkova, D.; Verellen, N.; Silhanek, A.V.; Valev, V.; Dorpe, P.V.; Moshchalkov, V.V. Mapping magnetic near-field distributions of plasmonic nanoantennas. *ACS Nano* **2013**, *7*, 3168–3176. [[CrossRef](#)] [[PubMed](#)]
12. Novotny, L.; Pohl, D.W.; Hecht, B. Scanning near-field optical probe with ultrasmall spot size. *Opt. Lett.* **1995**, *20*, 970. [[CrossRef](#)] [[PubMed](#)]
13. Bek, A.; Vogelgesang, R.; Kern, K. Apertureless scanning near-field optical microscope with sub-10 nm resolution. *Rev. Sci. Instrum.* **2006**, *77*, 043703. [[CrossRef](#)]
14. Zenhausern, F.; O'Boyle, M.P.; Wickramasinghe, H.K. Apertureless near-field optical microscope. *Appl. Phys. Lett.* **1994**, *65*, 1623. [[CrossRef](#)]
15. Hecht, B.; Bielefeldt, H.; Inouye, Y.; Pohl, D.; Novotny, L. Facts and artifacts in near-field optical microscopy. *J. Appl. Phys.* **1997**, *81*, 2492. [[CrossRef](#)]
16. Lereu, A.; Passian, A.; Dumas, P. Near-field optical microscopy: A brief review. *Int. J. Nanotechnol.* **2012**, *9*, 3–7. [[CrossRef](#)]
17. Zhang, W.; Fang, Z.; Zhu, X. Near-field Raman spectroscopy with aperture tips. *Chem. Rev.* **2017**, *117*, 5095–5109. [[CrossRef](#)] [[PubMed](#)]
18. Li, J.F.; Huang, Y.F.; Ding, Y.; Yang, Z.L.; Li, S.B.; Zhou, X.S.; Fan, F.R.; Zhang, W.; Zhou, Z.Y.; Wu, D.Y.; et al. Shell-isolated nanoparticle-enhanced Raman spectroscopy. *Nature* **2010**, *464*, 392–395. [[CrossRef](#)] [[PubMed](#)]
19. Kulzer, F.; Orrit, M. Single-molecule optics. *Annu. Rev. Phys. Chem.* **2004**, *55*, 585. [[CrossRef](#)] [[PubMed](#)]
20. Baschè, T.; Moerner, W.E.; Orrit, M.; Wild, U.P. *Single-Molecule Optical Detection, Imaging and Spectroscopy*; VCH: Weinheim, Germany, 1997. [[CrossRef](#)]
21. Tsien, R.Y.; Waggoner, A. Fluorophores for confocal microscopy: Photophysics and photochemistry. In *Handbook of Biological Confocal Microscopy*; Springer: New York, NY, USA, 2006; pp. 338–352.
22. Tsien, R.Y. The green fluorescent protein. *Annu. Rev. Biochem.* **1998**, *67*, 509. [[CrossRef](#)] [[PubMed](#)]
23. Stevenson, R.; Milner, R.G.; Richards, D.; Arias, A.C.; Mackenzie, J.D.; Halls, J.J.M.; Friend, R.H.; Kang, D.-J.; Blamire, M. Fluorescence scanning near-field optical microscopy of polyfluorene composite. *J. Microsc.* **2001**, *202*, 433–438. [[CrossRef](#)]
24. Müller-Zülow, B.; Kämmer, S.; Gehring, S.; Reineke, F. Fluorescence and luminescence testing of electronical devices with SNOM. *Microelectron. Eng.* **1996**, *31*, 163–168. [[CrossRef](#)]
25. Freudiger, C.W.; Min, W.; Saar, B.G.; Lu, S.; Holtom, G.R.; He, C.; Tsai, J.C.; Kang, J.X.; Xie, X.S. Label-free biomedical imaging with high sensitivity by stimulated Raman scattering microscopy. *Science* **2008**, *322*, 1857. [[CrossRef](#)] [[PubMed](#)]
26. Pashaee, F.; Sharifi, F.; Fanchini, G.; Lagugné-Labarthe, F. Tip-enhanced Raman spectroscopy of graphene-like and graphitic platelets on ultraflat gold nanoplates. *Phys. Chem. Chem. Phys.* **2015**, *17*, 21315. [[CrossRef](#)] [[PubMed](#)]
27. Ayas, S.; Cinar, G.; Ozkan, A.D.; Soran, Z.; Ekiz, O.; Kocaay, D.; Tomak, A.; Toren, P.; Kaya, Y.; Tunc, I.; et al. Label-free nanometer-resolution imaging of biological architectures through surface enhanced Raman scattering. *Sci. Rep.* **2013**, *3*, 2624. [[CrossRef](#)] [[PubMed](#)]
28. Ouyang, T.; Akbari-Sharbat, A.; Park, J.; Bauld, R.; Cottam, M.G.; Fanchini, G. Self-assembled metallic nanoparticle superlattices on large-area graphene thin films: Growth and evanescent waveguiding properties. *RSC Adv.* **2015**, *5*, 98814–98821. [[CrossRef](#)]
29. Le Feber, B.; Rotenberg, N.; Beggs, D.M.; Kuipers, L. Simultaneous measurement of nanoscale electric and magnetic optical fields. *Nat. Photonics* **2014**, *8*, 43–46. [[CrossRef](#)]
30. Rotenberg, N.; Krijger, T.L.; le Feber, B.; Spasenović, M.; Javier García de Abajo, F.; Kuipers, L. Magnetic and electric response of single subwavelength holes. *Phys. Rev. B* **2013**, *88*, 241408(R). [[CrossRef](#)]
31. Rotenberg, N.; Spasenović, M.; Krijger, T.L.; le Feber, B.; de Abajo, F.G.; Kuipers, L. Plasmon scattering from single subwavelength holes. *Phys. Rev. Lett.* **2012**, *108*, 127402. [[CrossRef](#)] [[PubMed](#)]
32. Burrese, M.; van Oosten, D.; Kampfrath, T.; Schoenmaker, H.; Heideman, R.; Leinse, A.; Kuipers, L. Probing the magnetic field of light at optical frequencies. *Science* **2009**, *326*, 550–553. [[CrossRef](#)] [[PubMed](#)]

33. Denkova, D.; Verellen, N.; Silhanek, A.V.; van Dorpe, P.; Moshchalkov, V.V. Lateral magnetic near-field imaging of plasmonic nanoantennas with increasing complexity. *Small* **2014**, *10*, 1959–1966. [[CrossRef](#)] [[PubMed](#)]
34. Kihm, H.W.; Kim, J.; Koo, S.; Ahn, J.; Ahn, K.; Lee, K.; Park, N.; Kim, D.-S. Optical magnetic field mapping using a subwavelength aperture. *Opt. Exp.* **2013**, *21*, 5625–5633. [[CrossRef](#)] [[PubMed](#)]
35. Schnell, M.; García-Etxarri, A.; Alkorta, J.; Aizpurua, J.; Hillenbrand, R. Phase-resolved mapping of the near-field vector and polarization state in nanoscale antenna gaps. *Nano Lett.* **2010**, *10*, 3524–3528. [[CrossRef](#)] [[PubMed](#)]
36. Koenderink, A.F.; Kafesaki, M.; Buchler, B.C.; Sandoghdar, V. Controlling the resonance of a photonic crystal microcavity by a near-field probe. *Phys. Rev. Lett.* **2005**, *95*, 153904. [[CrossRef](#)] [[PubMed](#)]
37. Lalouat, L.; Cluzel, B.; Velha, P.; Picard, E.; Peyrade, D.; Hugonin, J.P.; Lalanne, P.; Hadji, E.; de Fornel, F. Near-field interactions between a subwavelength tip and a small-volume photonic-crystal nanocavity. *Phys. Rev. B* **2007**, *76*, 041102(R). [[CrossRef](#)]
38. Chen, J.; Badioli, M.; Alonso-González, P.; Thongrattanasiri, S.; Huth, F.; Osmond, J.; Spasenović, M.; Centeno, A.; Pesquera, A.; Godignon, P.; et al. Optical nano-imaging of gate-tunable graphene plasmons. *Nature* **2012**, *487*, 77–81. [[CrossRef](#)] [[PubMed](#)]
39. Chorsi, H.T.; Zhang, J.X.J. Apertureless near-field scanning probes based on graphene plasmonics. *IEEE Photonics J.* **2017**, *9*, 4800207. [[CrossRef](#)]
40. Kauranen, M.; Zayats, A.V. Nonlinear plasmonics. *Nat. Photonics* **2012**, *6*, 737–748. [[CrossRef](#)]
41. Ikeda, S.; Cai, Y.; Meng, Q.; Yokoyama, T.; Shinozaki, K.; Komatsu, T.; Ishibashi, T. Imaging of localized surface plasmon by apertureless scanning near-field optical microscopy. *Sens. Mater.* **2015**, *27*, 985–991.
42. Amenabar, I.; Poly, S.; Nuansing, W.; Hubrich, E.H.; Govyadinov, A.A.; Huth, F.; Krutokhvostov, R.; Zhang, L.; Knez, M.; Heberle, J.; et al. Structural analysis and mapping of individual protein complexes by infrared nanospectroscopy. *Nat. Commun.* **2013**, *4*, 2890. [[CrossRef](#)] [[PubMed](#)]
43. Huth, F.; Schnell, M.; Wittborn, J.; Ocelic, N.; Hillenbrand, R. Infrared-spectroscopic nanoimaging with a thermal source. *Nat. Mater.* **2011**, *10*, 352–356. [[CrossRef](#)] [[PubMed](#)]
44. Jones, A.C.; Raschke, M.B. Thermal infrared near-field spectroscopy. *Nano Lett.* **2012**, *12*, 1475–1481. [[CrossRef](#)] [[PubMed](#)]
45. Westermeier, C.; Cernescu, A.; Amarie, S.; Liewald, C.; Keilmann, F.; Nickel, B. Sub-micron phase coexistence in small-molecule organic thin films revealed by infrared nano-imaging. *Nat. Commun.* **2014**, *5*, 4101. [[CrossRef](#)] [[PubMed](#)]
46. Umeda, N.; Hayashi, Y.; Nagai, K.; Takayanagi, A. Scanning wiener-fringe microscope with an optical fiber tip. *Appl. Opt.* **1992**, *31*, 4515–4518. [[CrossRef](#)] [[PubMed](#)]
47. Bacsá, W.; Levine, B.; Caumont, M. Local optical field variation in the neighborhood of a semiconductor micrograting. *J. Opt. Soc. Am. B* **2006**, *23*, 893–896. [[CrossRef](#)]
48. Ezugwu, S.; Yea, H.; Fanchini, G. Three-dimensional scanning near-field optical microscopy (3D-SNOM) imaging of random arrays of copper nanoparticles: Implications for plasmonic solar cell enhancement. *Nanoscale* **2015**, *7*, 252–260. [[CrossRef](#)] [[PubMed](#)]
49. Martínez-Marrades, A.; Greusard, L.; de Wilde, Y.; Bardou, N.; Collin, S.; Guillon, M.; Tessier, G. Characterization of plasmonic nano antennas by holographic microscopy and scanning near-field microscopy. *Opt. Commun.* **2016**, *359*, 455–459. [[CrossRef](#)]
50. Li, Y.; Zhou, N.; Raman, A.; Xu, X. Three-dimensional mapping of optical near-field with scattering SNOM. *Opt. Exp.* **2015**, *23*, 18730–18735. [[CrossRef](#)] [[PubMed](#)]
51. Guo, R.; Kinzel, E.C.; Li, Y.; Uppuluri, S.M.; Raman, A.; Xu, X. Three-dimensional mapping of optical near-field of a nanoscale bowtie antenna. *Opt. Exp.* **2010**, *18*, 4961–4971. [[CrossRef](#)] [[PubMed](#)]
52. Zhou, N.; Li, Y.; Xu, X. Resolving near-field from high order signals of scattering near-field scanning optical microscopy. *Opt. Exp.* **2014**, *22*, 18715–18723. [[CrossRef](#)] [[PubMed](#)]
53. Olmon, R.L.; Rang, M.; Krenz, P.M.; Lail, B.A.; Saraf, L.V.; Boreman, G.L.; Raschke, M.B. Determination of electric-field, magnetic-field, and electric-current distributions of infrared optical antennas: A near-field optical vector network analyzer. *Phys. Rev. Lett.* **2010**, *105*, 167403. [[CrossRef](#)] [[PubMed](#)]
54. Bauld, R.; Hesari, M.; Workentin, M.S.; Fanchini, G. Thermal stability of Au<sub>25</sub><sup>−</sup> Molecular precursors and nucleation of gold nanoparticles in thermosetting polyimide thin films. *Appl. Phys. Lett.* **2012**, *101*, 243114. [[CrossRef](#)]

55. Costantini, D.; Greusard, L.; Bousseksou, A.; Rungsawang, R.; Zhang, T.P.; Callard, S.; Decobert, J.; Lelarge, F.; Duan, G.-H.; de Wilde, Y.; et al. In situ generation of surface plasmon polaritons using a near-infrared laser diode. *Nano Lett.* **2012**, *12*, 4693–4697. [[CrossRef](#)] [[PubMed](#)]
56. Liu, M.; Wagner, M.; Zhang, J.; McLeod, A.; Kittiwatanakul, S.; Fei, Z.; Abreu, E.; Goldflam, M.; Sternbach, A.J.; Dai, S.; et al. Symmetry breaking and geometric confinement in VO<sub>2</sub>: Results from a threedimensional infrared nano-imaging. *Appl. Phys. Lett.* **2014**, *104*, 121905. [[CrossRef](#)]
57. Bulat, K.; Rygula, A.; Szafraniec, E.; Ozaki, Y.; Baranska, M. Live endothelial cells imaged by scanning near-field optical microscopy (SNOM): Capabilities and challenges. *J. Biophotonics* **2017**, *10*, 928–938. [[CrossRef](#)] [[PubMed](#)]
58. Klein, A.E.; Janunts, N.; Schmidt, S.; Hasan, S.B.; Etrich, C.; Fasold, S.; Kaiser, T.; Rockstuhl, C.; Pertsch, T. Dual-SNOM investigations of multimode interference in plasmonic strip waveguides. *Nanoscale* **2017**, *9*, 6695–6702. [[CrossRef](#)] [[PubMed](#)]
59. Garcia, M.A. Surface plasmons in metallic nanoparticles: Fundamentals and applications. *J. Phys. D Appl. Phys.* **2011**, *44*, 283001. [[CrossRef](#)]
60. Hecht, B.; Bielefeldt, H.; Novotny, L.; Inouye, Y.; Pohl, D.W. Local excitation, scattering, and interference of surface plasmons. *Phys. Rev. Lett.* **1996**, *77*, 1889. [[CrossRef](#)] [[PubMed](#)]
61. Kim, H.J.; Ji, W.S.; O, B.-h.; Park, S.; Lee, E.-H.; Lee, S.G. Characterization of a focusing waveguide grating coupler using a bloch-wave analysis-based local linear grating model and near-field scanning optical microscope. *J. Korean Phys. Soc.* **2005**, *46*, 1013–1019.
62. Cheon, S.; Kihm, K.; Kim, H.; Lim, G.; Park, J.S.; Lee, J.S. How to reliably determine the complex refractive index (RI) of graphene by using two independent measurement constraints. *Sci. Rep.* **2014**, *4*, 6364. [[CrossRef](#)] [[PubMed](#)]



© 2017 by the authors. Licensee MDPI, Basel, Switzerland. This article is an open access article distributed under the terms and conditions of the Creative Commons Attribution (CC BY) license (<http://creativecommons.org/licenses/by/4.0/>).